Direct measurement of the $\bar{K}N \to \pi\Sigma$ scattering amplitude below the $\bar{K}N$ threshold employing the $d(K^-, N)"\pi\Sigma"$ reaction

Kentaro Inoue

November 28, 2025

Contents

Chapter 1

Introduction

Chapter 2

Experimental setup

Chapter 3

Analysis

Chapter 4

$\pi\Sigma$ Spectra

4.1 Decomposition of the $K^- d \to n\pi^+\pi^- n$ events

4.1.1 Backward $\pi^\mp\Sigma^\pm$ event selection

4.1.2 Template fitting

4.2 Conversion to the cross section

4.2.1 Acceptance correction

4.2.2 Conversion factors for the cross section

Chapter 5

Discussion

5.1 Spectra

5.1.1 Qualitative properties of obtained spectra

The $d(K^-, n)\pi^\mp\Sigma^\pm$ and $d(K^-, p)\pi^-\Sigma^0$ spectra obtained through the procedures described in the previous section are shown together in Figure 5.1. In this figure, the green vertical line indicates the $\bar{K}N$ threshold. This section discusses the qualitative features of the obtained spectra.

The experiment is interpreted as a two-step reaction, as described in Section 1.7. The $\pi^-\Sigma^0$ spectrum contains only the $I = 1$ component from the second-step scattering, and this second-step scattering does not exhibit a significant structure, as there is no pole near the $\bar{K}N$ threshold. As a result, the $\bar{K}N$ spectrum reflects the first-step scattering more directly. A bump-like shape emerges from the $\bar{K}N$ threshold due to the Fermi motion of the spectator.

For the $I = 0$ component, the second-step scattering is expected to exhibit a pronounced structure below the $\bar{K}N$ threshold due to the presence of poles in that region. This results in a spectral shape with a stronger enhancement below the $\bar{K}N$ threshold compared to the bump-like feature originating from the first-step scattering. Indeed, the observed $\pi^\mp\Sigma^\pm$ spectra, which contain both $I = 0$ and $I = 1$ components as well as their interference, exhibit a clear structure below the $\bar{K}N$ threshold. The overall spectral intensity is also larger than that of the $\pi^-\Sigma^0$ spectrum, which only contains the $I = 1$ component, due to the pole contribution in the $I = 0$ channel. The interference between the $I = 0$ and $I = 1$ components appears as a difference between the $\pi^-\Sigma^+$ and $\pi^+\Sigma^-$ spectra. Since the measured spectra show a clear asymmetry between them, the interference effect be-
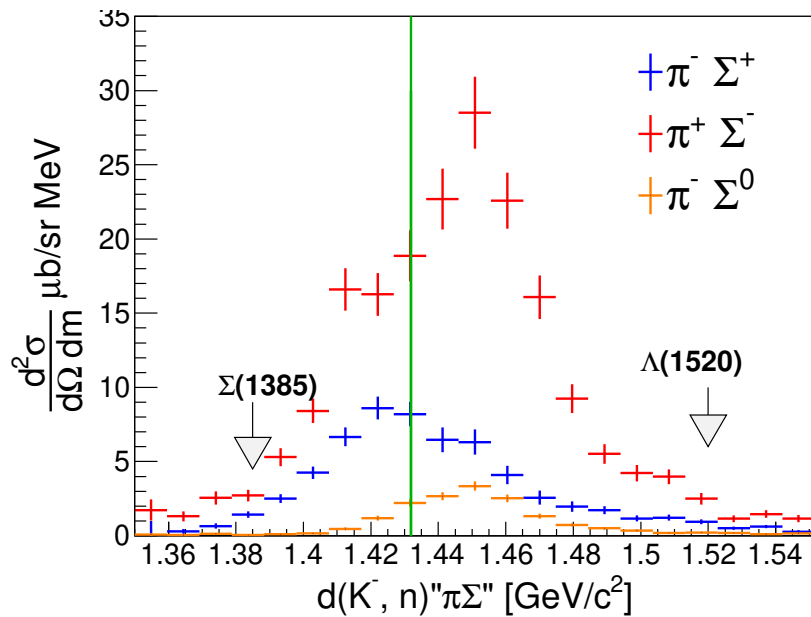
Figure 5.1: The obtained cross sections are plotted simultaneously in this figure. The $d(K^-, n)"\pi^-\Sigma^+$, $d(K^-, n)"\pi^+\Sigma^-"$, $d(K^-, n)"nK^{0}"$, and $d(K^-, p)"\pi^-\Sigma^{0}"$ plot as red, blue, green, and orange, lines respectively. The $d(K^-, n)"nK^{0}"$ is scaled to $1/10$. The green virtical line indicates the $\bar{K}N$ threshold.

tween $I = 0$ and $I = 1$ was observed in the reactions in this experiment.

In the second-step scattering near the $\bar{K}N$ threshold, S-waves are expected to dominate due to the small angular momentum transfer transfer. However, it is well known that in this region there are $I = 0$ D-wave resonances, such as the $\Lambda(1520)$, and $I = 1$ P-wave resonances, such as the $\Sigma(1385)$. The absence of structures around the $\Sigma(1385)$ region in the measured $I = 1$ $\pi^-\Sigma^0$ spectrum, as well as around both the $\Sigma(1385)$ and $\Lambda(1520)$ regions in the $\pi^+\Sigma^-$ and $\pi^-\Sigma^+$ spectra with mixed $I = 0$ and $I = 1$ contributions, confirms that the S-wave dominates in the reactions observed in this experiment.

5.1.2   Comparison with theoritical calculations

The previous section discussed the qualitative features of the obtained spectra. In this section, we examine how well the reaction can be understood by comparing the data with theoretical calculations that take into account the kinematics of this experiment.

Two theoretical calculations are used for this purpose. One is the *hybrid* calculation by Miyagawa et al., which separates the reaction into a first-step high-energy $K^-N \to \bar{K}N$ scattering and a second-step low-energy $\bar{K}N \to \pi\Sigma$ scattering, which is the main focus. In the second-step, three different scattering amplitudes obtained from various analyses of the $\Lambda(1405)$ are used. This is to say, this method allows the second-step scattering amplitudes to be substituted with results from any $\Lambda(1405)$ analysis. The other method is the DCC method, which treats these energy regions in a unified manner and uses continuous scattering amplitudes for both scatterings. In this method, there are two sets of datasets, A and B, with the main uncertainty due to the lack of scattering data in the low energy region.

Figure 5.2 shows a comparison between the experimental data and the predicted spectra from theoretical calculations. The theoretical spectra are convolved with the detector resolution described in Appendix **??**. From top to bottom, the $\pi^+\Sigma^-$, $\pi^-\Sigma^+$, and $\pi^-\Sigma^0$ spectra are shown. The right column shows the results from the DCC method [46], and the left column shows those from the *hybrid* calculation by Miyagawa et al [42].

The spectral shapes calculated by the two theoretical methods reproduce well the qualitative features discussed in the previous section. Specifically, the $\pi^-\Sigma^0$ spectrum with an $I = 1$ contribution exhibits a bump structure reflecting the first-step scattering, while the $\pi^\mp\Sigma^\pm$ spectra, which include $I = 0$, $I = 1$, and their interference components, show a clear structure below the $\bar{K}N$ threshold. The difference observed between the $\pi^+\Sigma^-$ and
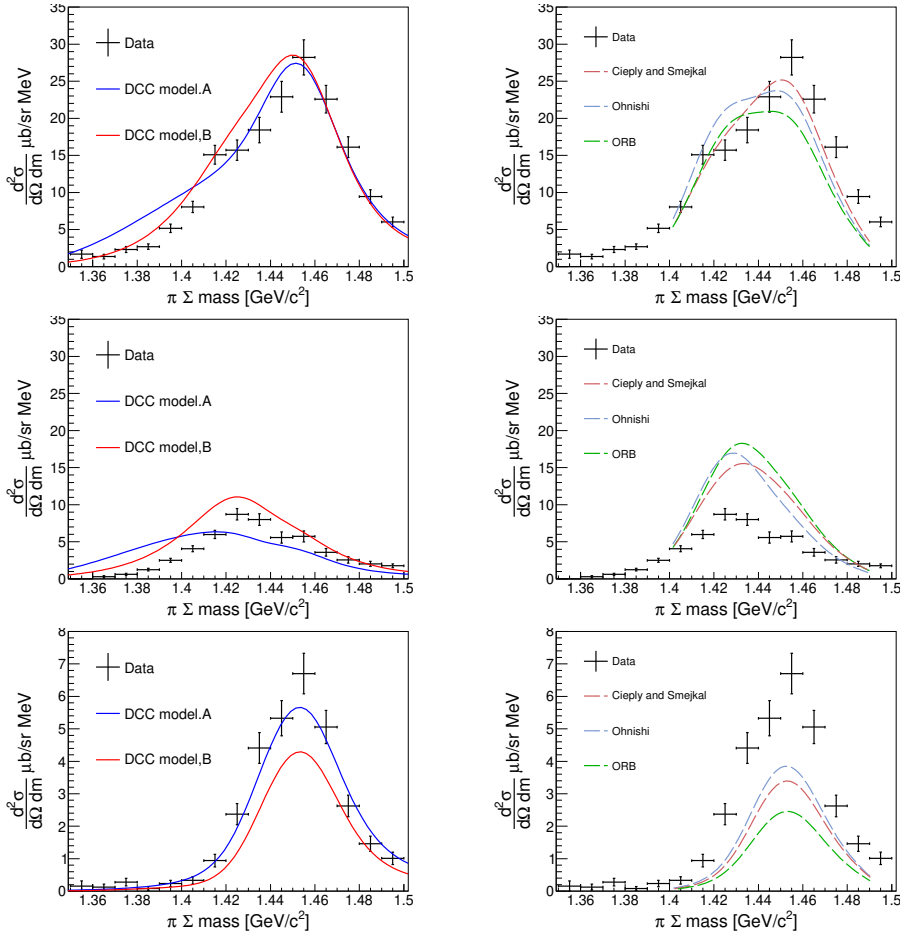
Figure 5.2: This figure shows a comparison of our obtained spectra with predictions from theoretical calculations. The top, middle, and bottom figures represent $\pi^-\Sigma^+$, $\pi^+\Sigma^-$, and $\pi^-\Sigma^0$, respectively. The right figure shows the spectrum predicted by the DCC model [46], and the left figure shows the spectrum predicted by the calculation of Miyagawa et al [42]. The spectra predicted by theoretical calculations are convoluted with our detector resolution.

$\pi^-\Sigma^+$ spectra, which originates from the interference between the $I = 0$ and $I = 1$ components, is also reasonably well reproduced by the calculations.

However, the spectra predicted by the DCC method are well reproduced, both in shape and intensity. In contrast, the *hybrid* calculation reasonably reproduces the $\pi^+\Sigma^-$ spectrum in both shape and intensity, but significantly overestimates the intensity of the $\pi^-\Sigma^+$ spectrum and underestimates that of the $\pi^-\Sigma^0$ spectrum.

This implies that a continuous treatment of the first- and second-step scattering is essential for understanding the present reaction. That is to say, consistency with the higher-energy region is important for understanding $\bar{K}N$ scattering in the $\Lambda(1405)$ region.

The following discussion focuses on the spectra calculated by the DCC method.

Here, the spectra are decomposed into the $I = 0$, $I = 1$, and interference components in order to clarify the contriutions of these factors. The obtained spectrum can be expressed as follows from the isospin relation.

$$\frac{d\sigma}{d\Omega dM}(\pi^\mp\Sigma^\pm) \propto \left| C^0_{K^-N\to\bar{K}N} T^{I=0}_{\bar{K}N\to\pi\Sigma} \mp C^1_{K^-N\to\bar{K}N} T^{I=1}_{\bar{K}N\to\pi\Sigma} \right|^2$$
$$= \left| C^0_{K^-N\to\bar{K}N} T^{I=0}_{\bar{K}N\to\pi\Sigma} \right|^2 + \left| C^1_{K^-N\to\bar{K}N} T^{I=1}_{\bar{K}N\to\pi\Sigma} \right|^2$$
$$\mp 2\mathrm{Re}(C^0_{K^-N\to\bar{K}N} C^1_{K^-N\to\bar{K}N} T^{I=0}_{\bar{K}N\to\pi\Sigma} T^{I=1}_{\bar{K}N\to\pi\Sigma}) \qquad (5.1)$$
$$\frac{d\sigma}{d\Omega dM}(\pi^-\Sigma^0) \propto \left| C^1_{K^-N\to\bar{K}N} T^{I=1}_{\bar{K}N\to\pi\Sigma} \right|^2 \qquad (5.2)$$

Here, $T^{I=0,1}_{\bar{K}N\to\pi\Sigma}$ represents the T matrix of the second $\bar{K}N \to \pi\Sigma$ scattering for isospin $I = 0$ and $I = 1$. Additionally, $C^{0,1}_{K^-N\to\bar{K}N}$ denotes the factor for the first $K^-p \to \bar{K}N$ scattering, corresponding to the isospin $I = 0$ and $I = 1$ components of the second scattering.

Since it can be expressed as shown in Equation (5.1), (5.2), the spectra corresponding to $I = 0$, $I = 1$, and their interference terms can be written

as follows.

$$\frac{d\sigma}{d\Omega dM}(I=0) \propto \frac{1}{2}\left(\frac{d\sigma}{d\Omega dM}(\pi^-\Sigma^+) + \frac{d\sigma}{d\Omega dM}(\pi^+\Sigma^-) - \frac{d\sigma}{d\Omega dM}(\pi^-\Sigma^0)\right)$$

$$= \left|C^0_{K^-N\to\bar{K}N}T^{I=0}_{\bar{K}N\to\pi\Sigma}\right|^2 \tag{5.3}$$

$$\frac{d\sigma}{d\Omega dM}(I=1) \propto \frac{d\sigma}{d\Omega dM}(\pi^-\Sigma^0)$$

$$= \left|C^1_{K^-N\to\bar{K}N}T^{I=1}_{\bar{K}N\to\pi\Sigma}\right|^2 \tag{5.4}$$

$$\frac{d\sigma}{d\Omega dM}(int) \propto \left(\frac{d\sigma}{d\Omega dM}(\pi^-\Sigma^+) - \frac{d\sigma}{d\Omega dM}(\pi^+\Sigma^+)\right)$$

$$= 4\mathrm{Re}(C^0_{K^-N\to\bar{K}N}C^2_{K^-N\to\bar{K}N}T^{I=0}_{\bar{K}N\to\pi\Sigma}T^{I=1}_{\bar{K}N\to\pi\Sigma}) \tag{5.5}$$

The spectrum is transformed according to this formula. We introduce scaling parameters $S_{I=0}$ and $S_{I=1}$ to adjust the intensities of the $I=0$ and $I=1$ components, respectively, so that the overall spectral shape becomes more comparable to the theoretical spectrum. The interference terms are scaled by $\sqrt{S_{I=0}S_{I=1}}$, as described in Equation 5.5.

Table 5.1: This table shows the pole position with $I=0$ and $J^P = 1/2^-$ below the $\bar{K}N$ threshold by DCC models [46]

	pole1	pole2
Model.A	$1437 - 75i$	$1372 - 56i$
Model.B	$1428 - 31i$	$1397 - 98i$

By fitting with these parameters, we obtain $S_{I=0} = 0.562 \pm 0.015$ and $S_{I=1} = 1.070 \pm 0.040$ for Model A, and $S_{I=0} = 0.721 \pm 0.016$ and $S_{I=1} = 1.423 \pm 0.055$ for Model B. The results of these fits are shown in the Fig.5.3 : the left panel corresponds to Model A, and the right panel to Model B. The top subpanels show the spectra for the $I=0$ component, the middle ones for the $I=1$ component (i.e., the $\pi^-\Sigma^0$ spectrum), and the bottom ones for the interference term.

In Model B (right panel), a reasonably good agreement is observed across all spectra. In contrast, Model A (left panel) reproduces the central $I=1$ term well, but the upper $I=0$ and lower interference terms appear to be underestimated in the fit results in the quasi-elastic scattering region. Indeed, the χ^2/NDF values are $220/42 = 5.25$ for Model B and $691/42 = 16.4$ for Model A, indicating a significantly better fit for Model B. This discrepancy is considered to arise from the fact that the theoretical spectrum
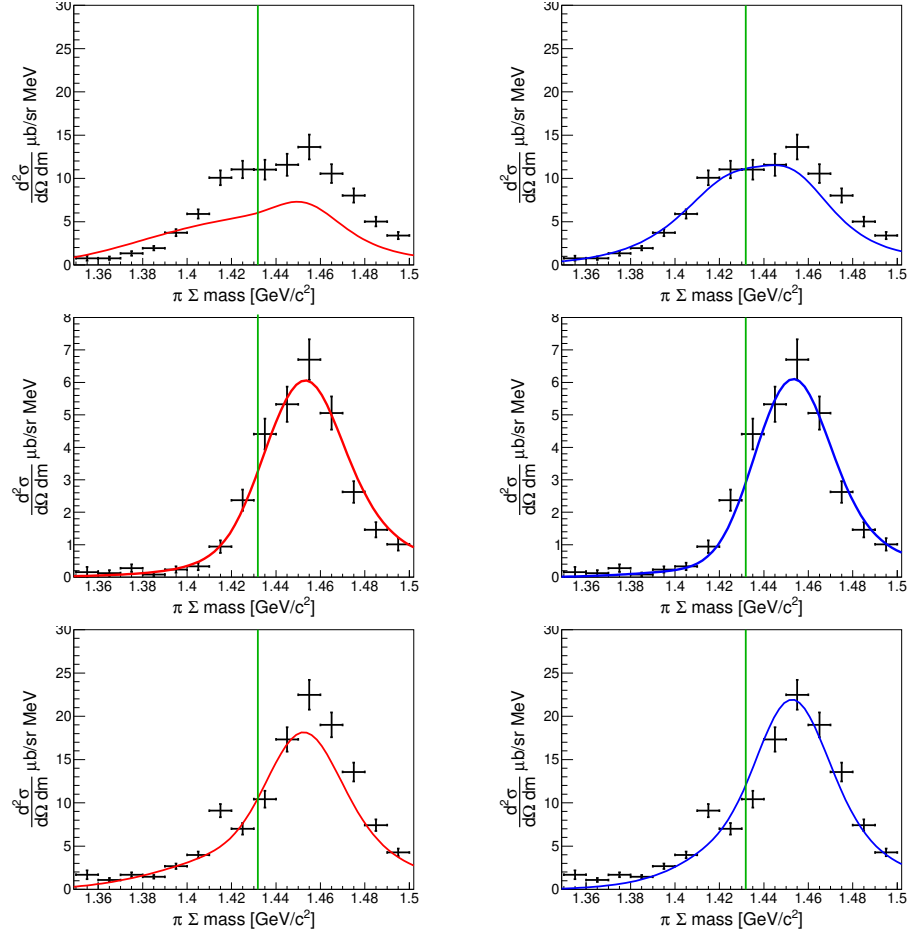
Figure 5.3:   This figure illustrates the spectra of the experimental data, decomposed into $I = 0$, $I = 1$, their interference terms, and the corresponding fitting results obtained using Model A of the DCC model. The black error bars represent the experimental data, while the red line denotes the fit results. The upper-left panel corresponds to $I = 0$, the upper-right panel to $I = 1$, and the lower panel to the interference term.

for $I = 0$ possesses a long-tailed component in the bound region. Table 5.1 summarizes the parameters of the $I = 0$ pole used in the theoretical calculations for the fit. This is attributed to the large imaginary part of pole 1, which is strongly coupled to the $\bar{K}N$ channel and therefore has a pronounced effect in this experiment.

As shown in Eq.(5.5), the phase difference between $I = 0$ and $I = 1$ modifies the interference term. We demonstrate that introducing this phase difference as a fitting parameter leads to an improved fit. The following discussion focuses exclusively on Model B, which provided the better overall agreement. Since the $I = 1$ component is determined solely from the experimental spectrum, two fitting strategies can be considered (i) first fixing the $I = 1$ contribution by $\pi^- \Sigma^0$ spectrum, or (ii) fitting all spectra simultaneously. The results obtained from these two approaches are presented in Fig. 5.4 and 5.5.

5.1.3 $\bar{K}N$ Pole parameters assuming the 2-step reaction
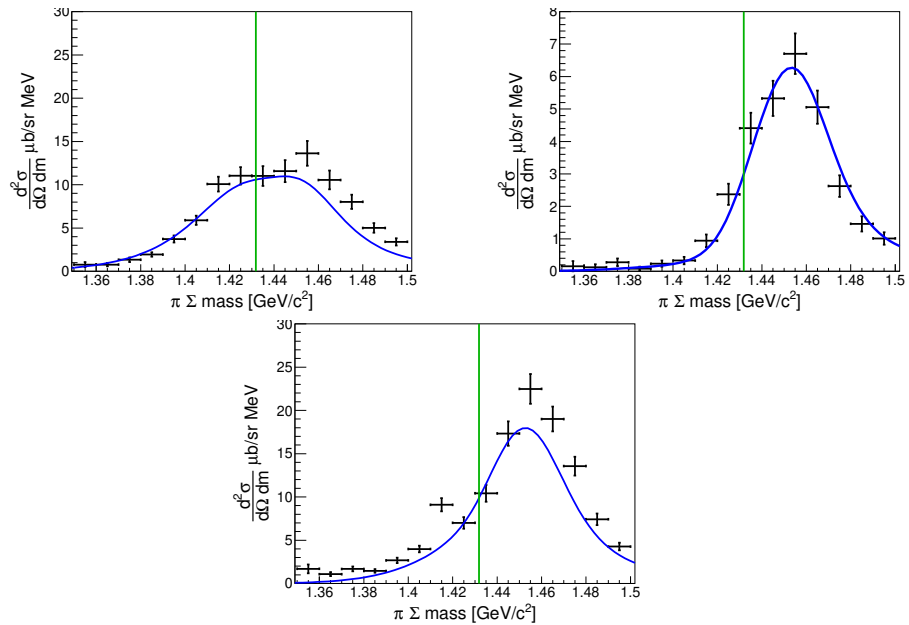
Figure 5.4:   This figure shows the fitting results obtained when the degrees of freedom associated with the interference term are introduced as additional fitting parameters. The upper-left panel displays the $I = 0$ component, the upper-right panel shows the $I = 1$ component, and the lower panel presents the spectrum of the interference term. The error bars denote the experimental data, while the blue curve represents the fit obtained using DCC Model B. In this figure, the $I = 1$ strength is determind by the only $\pi^- \Sigma^0$ spectrum.
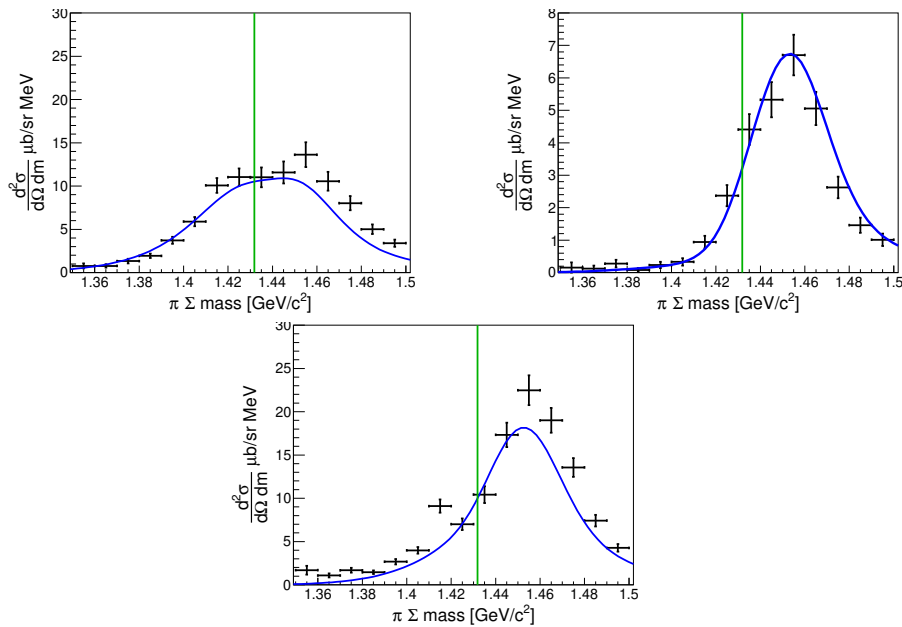
Figure 5.5:   This figure, similar to Fig. **??**, includes the fitting parameters for the interference term; however, in this case, the spectrum is determined by simultaneously fitting the $\pi^{\mp}\Sigma^{\pm}$ and $\pi^{-}\Sigma^{0}$ channels.

Chapter 6

Conclusion

Appendix A

$\pi^0\Sigma^0$ spectrum analysis

Appendix B

Detector resolution

The resolution of the final $\pi\Sigma$ spectrum can be categorized into two main sources: one originating from the CDS and the other from the forward detector system. The resolution of each detector was estimated by reproducing the mass distribution of known particles measured in our experiments, and these values were used to estimate the resolution of the final pi-Sigma spectrum.

B.1   CDC resolution
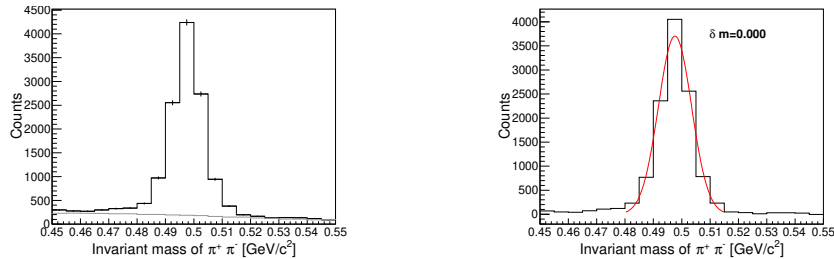
Figure B.1:   These figures show the $K^0 \to \pi^+\pi^-$ decay peak in $K^-d \to n\pi^+\pi^n$ events. The left figure displays the $K^-d \to n\pi^+\pi^-n$ event spectrum (black line) along with the MC simulated background (gray line). The right figure presents the background-subtracted spectra and the fit results.

As explained in Section ??, the CDS measures the momentum of charged particles by tracking their trajectories in a magnetic field. The resolution of the CDS is estimated using events in which the K^0 produced in the $K^-d \to nnK^0$ reaction decays into π^+ and π^-. This reaction is one of the
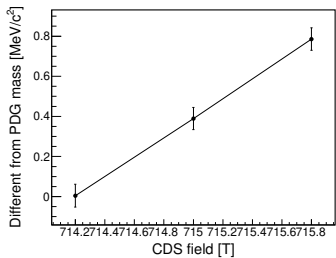
Figure B.2: This figure shows the relationship between the magnetic field settings of the CDC in the analysis and the center value of the K^0 peak.

$K^- d \to n\pi^+\pi^- n$ final states described in Section 4.1, and this final state is fully reconstructed as explained in Section 4.1.2. Therefore, by subtracting reactions other than K^0 production, only the peak can be extracted, as shown in Figure. B.1 The magnetic field of the CDS is measured using a Hall probe, and fine-tuning is performed based on the K^0 peak. As shown in the Figure B.2, this was done using selected values of the CDS magnetic field applied in the experimental data analysis. The field was slightly adjusted from the default value of ???T and was finally determined to be ???T.

The momentum resolution is based on the positional resolution of the CDC. To determine the positional resolution that best reproduces the width of the observed K^0 peak, the correlation between the positional resolution of the CDC and the width of the K^0 peak in the MC simulation was examined, as shown in Figure **??**. From this, the positional resolution was estimated to be $200\mu m$.

B.2   Detector resolution on the $d(K^-, N)$

Appendix C

$d(K^-, n)K^0 n$ analysis

Bibliography

[1] R.L. Workman et al. (Particle Data Group), Prog. Theor. Exp. Phys. 2022, 083C01 (2022)
    "Review of Particle Physics"

[2] R. H. Dalitz and A. Deloff, J. Phys. G17, 281 (1991).
    "The Shape and Parameters of the $\Lambda(1405)$ Resonance"

[3] M. Hassanvand et el., Phys. Rev. C **87**, 055202 (2013)
    "Theoretical analysis of $\Lambda(1405) \rightarrow (\pi\Sigma)^0$ mass spectra produced in $p + p \rightarrow p + \Lambda(1405) + p$ reactions"

[4] J. Esmaili, Y. Akaishi, and T. Yamazaki, Phys. Lett. B **686**, 23 (2010)
    "Experimental confirmation of the $\Lambda(1405)$ ansatz from resonant formation of a K^-p quasi-bound state in K^- absorption by ^{3}He and ^{4}He"

[5] R. H. Dalitz and S. F. Tuan, Phys. Rev. Lett. 2 (1959).
    "Possible Resonant State in Pion-Hyperon Scattering"

[6] M. H. Alston, L. W. Alvarez, P. Eberhard and M. L. Good,
    Phys. Rev. Lett. 6, 698 (1961).
    "Study of Resonances of the Σ-π System"

[7] R. J. Hemingway, Nucl Phys B **253**, 742 (1985).
    "Production of $\Lambda(1405)$ in K^-p Reactions at 4.2GeV/c"

[8] B. Conforto et el., Nucl. Phys. B **34**, 41 (1971).
    "New experimental results on the Reactions $K^-p \rightarrow \bar{K}N$ and $K^-p \rightarrow \Sigma\pi$ a partial-wave analysis between 430 and 800MeV/c"

[9] A. J. Van Horn, Nucl. Phys. B **87**, 145 (1975).
    "Energy dependent partial-wave analysis of $K^-p \rightarrow \Lambda\pi^0$ between1540 and 2215MeV"

[10] R. J. Hemingway et el., Nucl. Phys. B **91**, 12 (1975).
"New data on $K^-p \to K^-p$ and K^0n and a partial-wave analysis between 1840 and 2234MeV center of mass energy"

[11] P. Baillon and P. J. Litchfield, Nucl. Phys. B **94**, 39 (1975).
"Energy-independent partial-wave analysis of $\bar{K}N \to \Lambda\pi$ between 1540 and 2150 MeV"

[12] G. P. Gopal et al., Nucl. Phys. B **119**, 362 (1977).
"Partial-wave analyses of KN two-body reactions between 1480 and 2170 MeV"

[13] M. Sakitt et el., Phys. Rev. **139**, B179
"Low-Energy K^- Meson Interactions in Hydrogen"

[14] J. K. Kim, Phys. Rev. Lett. **19**, 1074 (1967).
"Multichannel Phase-Shift Analysis of $\bar{K}N$ Interaction in the Region 0 to 550 MeV/c"

[15] A. D. Martin, Nucl. Phys. B **179**, 33 (1981).
"Kaon-Nucleon Parameters"

[16] P. B. Siegel and W. Weise, Phys. Rev. C **38**, 2221 (1988).
"Low-energy K^--nucleon potentials and the nature of the $\Lambda(1405)$"

[17] J. D. Davies et al., Phys. Lett. B **83**, 55 (1979).
"Observation of kaonic hydrogen atom X-rays"

[18] M. Izycki et al., Z. Phys. A 297, 11 (1980).
"Results of the search for K-series X-rays from kaonic hydrogen"

[19] P. M. Bird et al., Nucl. Phys. A **404**, 482 (1983).
"Kaonic Hydrogen atom X-rays"

[20] M. Iwasaki et el., Phys. Rev. Lett. **78**, 3067 (1997).
"Observation of Kaonic Hydrogen K_α X Rays"

[21] M. Bazzi et el., Phys. Lett. B **704**, 113 (2011).
"A New Measuerment of Kaonic Hydrogen X-Rays"

[22] J.C.Nacher et el., Phys. Lett. B **455**, 55 (1999).
"Photoproduction of the $\Lambda(1405)$ on the proton and nuclei"

[23] M. Niiyama et el., Phys. Rev. C **78**, 035202 (2008).
"Photoproduction of $\Lambda(1405)$ and $\Sigma(1385)$ on the proton at $E_\gamma = 1.5$-$2.4\text{GeV}/c$"

[24] K. Moria for the CLAS Collaboration,
Phys. Rev. C **87**, 035206 (2013).
"Measurement of the $\pi\Sigma$ photoproduction line shapes near the $\Lambda(1405)$"

[25] K. Moria for the CLAS Collaboration,
Phys. Rev. Lett. **112**, 082004 (2014).
"Spin and parity measurement of the $\Lambda(1405)$ baryon"

[26] S. X. Nakamura, and D. Jido, Prog. Theor. Exp. Phys., 023D01 (2014)
"Lambda (1405) photoproduction based on the chiral unitary model"

[27] D. Jido et el., Nucl. Phys. A **725**, 181 (2003).
"Chiral Dynamics of the Two $\Lambda(1405)$ States"

[28] G. Agakishiev for the HADES Collaboration,
Phys. Rev C **87**, 025201 (2013).
"Baryonic Resonances to the $\bar{K}N$ threshold: The case of $\Lambda(1405)$ in pp collisions"

[29] Y. Ikeda, T. Hyodo, and W. Weise, Nucl. Phys. A **881**, 98 (2012)
"Chiral SU(3) theory of antikaon–nucleon interactions with improved threshold constraints"

[30] Z.-H. Guo and J. Oller, Phys. Rev. C **87**, 3, 035202 (2013)
"Meson-baryon reactions with strangeness   1 within a chiral framework"

[31] M. Mai and U.-G. Meißner, Eur. Phys. J. A **51**, 3, 30 (2015),
"Constraints on the chiral unitary amplitude from $\pi\Sigma K^+$ photoproduction data"

[32] H. Zhang et el., Phys. Rev. C **88**, 035204 (2013).
"Partial-wave analysis of $\bar{K}N$ scattering reactions"

[33] H. Zhang et el., Phys. Rev. C **88**, 035205 (2013).
"Multichannel parametrization of $\bar{K}N$ scattering amplitudes and extraction of resonance parameters"

[34] H. Kamano et el., Phys. Rev. C **90**, 065202 (2014).
"Dynamical Coupled-Channels Model of K^-p Reactions:

Determination of partial wave aamplitudes"
Phys. Rev. C**92**, 025205 (2015).
"Dynamical Coupled-Channels Model of K^-p Reactions.
Extraction of Λ^* and Σ^* Hyperon Resonances"
Phys. ReV. C**95**, 044903(E) (2015).

[35] G. Beer et el., Phys. Rev. Lett. **94**, 212302 (2005).
"Measurement of the Kaonic Hydrogen X-Ray Spectrum"

[36] S. Deser et el., Phys. Rev. **96**, 774 (1954).
"Energy Level Displacements in Pi-Mesonic Atoms"

[37] T.L. Trueman, Nucl. Phys. **26**, 57 (1961).
"Energy level shifts in atomic states of strongly-interacting particles"

[38] O. Braun et el., Nucl. Phys. B **129**, 1 (1977).
"New Information About the Kaon-Nucleon-Hyperon Coupling Constants $g(KN\Sigma(1197)), g(KN\Sigma(1385))$ and $g(KN\Lambda(1405))$"

[39] D. Jido, E. Oset and T. Sekihara, Eur. Phys. J. A **42**, 257 (2009).
"Kaonic Production of $\Lambda(1405)$ off deuteron target in chiral dynamics"

[40] J. Yamagata-Sekihara, T. Seki hara, and D. Jido, Prog. Theor. Exp. Phys.**2013**, 043D02 (2013).
"Production of hyperon resonances induced by kaons on a deuteron target"

[41] H. Noumi et el., Proposals for the 15th PAC meeting
"Spectroscopic study of hyperon resonances below $\bar{K}N$ threshold via the (K^-, n) reaction on Deuteron"

[42] K. Miyagawa, J. Haidenbauer, and H. Kamada Phys. Rev. C **97**, 055209 (2018)
"Faddev approach to the reaction $K - d \rightarrow \pi\Sigma n$ at $p_K = 1.0 GeV/c$"

[43] E. Oset, A. Ramos, and C. Bennhold, Phys. Lett. B **527**, 99 (2002); **530**, 260(E) (2002).
"Low lying $S = -1$ excited baryons and chiral symmetry"

[44] A. Cieplý and J. Smejkal, Nucl. Phys. A **881**, 115 (2012).
"Chirally motivated $\bar{K}N$ amplitudes for in-medium applications"

[45] S. Ohnishi et el, Phys. Rev. C **93**, 025207 (2016).
"Strcture of the $\Lambda(1405)$ and the $K^-d \to \pi\Sigma n$ reaction"

[46] H. Kamano et el., Phys. ReV. C**94**, 065205 (2016).
"Toward Establishing Low-Lying Λ and Σ Hyperon Resonances with the $\bar{K} + d \to \pi + Y + N$ Reaction"

[47] H. Noumi for the E31 Collaboration, Phys. ReV. B**837**, 137637 (2023).
"Pole Position of $\Lambda(1405)$ measured in $d(K^-, n)\pi\Sigma$ reaction"

[48] S. Kawasaki's Doctor thesis will be submitted.

[49] K. Agari et el, Prog. Theor. Exp. Phys., 02B009 (2012)

[50] K. Agari et el, Prog. Theor. Exp. Phys., 02B011 (2012)

[51] TRANSPORT http://linac96.web.cern.ch/Linac96/Proceedings/Thursday/THP72/Paper.pdf

[52] T. K. Ohska et al., Nuclear Science, IEEE Transactions on 33, 98 (1986).

[53] M. Shiozawa and et el., A new TKO system manager board for a dead-time-free data acquisition system, in 1994 IEEE Nuclear Science Symposium-NSS'94, pages 632–635, (1994)

[54] M. Iio et al., Nucl. Instrum. Methods Phys. Res., Sect. **A** 687, 1 (2012).

[55] S. Agostinelli et al., Nucl. Instrum. Methods Phys. Res., Sect. **A** 506, 250 (2003)
J. Allison et el., IEEE Transactions on Phys. Sci. 53, 207 (2006)
J.Allison et al., Nucl. Instrum. Methods Phys. Res., Sect. **A** 835, 186 (2016)

[56] K. Fuji, `https://www-jlc.kek.jp/subg/offl/lib/docs/helix_manip/node3.html` (1968).

[57] Opera Electromagnetic FEA Solution Software

[58] V. Flaminio et al., CERN-HARA-87-01, 121 (1983).

[59] M.Jones et el, Nucl. Phys. B **90**, 349 (1975)

[60] R. Barlow and C. Beeston, Comp. Phys. Comm. **77**, 219 (1993).
"Fitting using finite Monte Carlo samples"

[61] A. Nappi, Comp. Phys. Comm. **180**, 269 (2009).

[62] C.J.S. Damerell et. el., Ncul. Phys. B**129**, 397 (1977). "
     K^-n elastic scattering between 610 and 840 MeV/c"

[63] M. jones, R. Levi, Setti, D. Merrill and R. D. Tripp, Phys. Rev. B**90**,
     349 (1975). K^-p charge exchange and hyperon production cross section
     from 860 to 1000 MeV/c

[64] M. Bernheim and et. el., Nucl. Phys. A**365**, 349, (1981). Momentum
     distributions of nucleons in the deutron from $d(e, e'p)n$ reaction

[65] R. Machleidt, Phys. Rev. C**63**, 024001 (2001).

[66] R. Barlow and C. Beeston, Comp. Phys. Comm. **77**, 219 (1993).

[67] L. Lensniak, AIP Conf. Proc. 1030, 238–243 (2008). New formula for a
     resonant scattering near an inelastic threshold

[68] S. Agostinelli et al., Nuclear Instruments and Methods in Physics Re-
     search Section A: Accelerators, Spectrometers, Detectors and Associ-
     ated Equipment **506**, 250 (2003).
     J.Allison et el., Nuclear Instruments and Methods in Physics Re-
     search Section A: Accelerators, Spectrometers, Detectors and Associ-
     ated Equipment **835**, 186 (2016).